Delocalization of higher-order topological states in higher-dimensional non-Hermitian quasicrystals

Aoqian Shi,[1] Yuchen Peng,[1] Peng Peng,[1] Jianzhi Chen,[1] and Jianjun Liu[1,2,*]

[1]*Key Laboratory for Micro/Nano Optoelectronic Devices of Ministry of Education, School of Physics and Electronics, Hunan University, Changsha 410082, China*

[2]*Greater Bay Area Institute for Innovation, Hunan University, Guangzhou 511300, China*

(Received 7 April 2024; revised 30 June 2024; accepted 1 July 2024; published 16 July 2024)

The combination of the non-Hermitian skin effect (NHSE) and topological effects plays a crucial role in both fundamental and applied physics. Here, we show the interplay between the NHSE and topological effects in two- and three-dimensional quasicrystals. Unlike the delocalization of higher-order topological states (HOTSs) in crystals, we find that in non-Hermitian quasicrystals, HOTSs delocalize along the boundaries rather than in the bulk regions. Through effective analysis of the quasicrystal boundaries, we establish a physical connection between the unique lattice arrangement of quasicrystals and the delocalization of HOTSs. Our results offer some perspectives for investigating intriguing physical phenomena emerging from the combination of higher-dimensional quasicrystals, the NHSE, and topological effects, as well as for broadening their applications.

DOI: 10.1103/PhysRevB.110.014106

I. INTRODUCTION

Non-Hermitian system offers a novel approach for exploring topological physics [1], and the non-Hermitian skin effect (NHSE) presents unique mechanisms for localization of electrons, phonons, and photons [2–6]. Based on the NHSE, physical phenomena distinct from those in Hermitian systems have been realized [7–10], including non-Hermitian higher-order topological states (HOTSs), higher-order skin states, and hybrid higher-order skin-topological states. They have been experimentally verified in active matter [11], electric circuits [12,13], phononics [14], and photonics [15–17] and are promising for applications in topological sensors [11,12], reconfigurable laser arrays [15], and topological switches [12,16].

Previous works on the NHSE have emphasized the enhanced localization of bulk states and topological states, which corresponds to a dimensionality reduction of the wave function distribution from higher to lower dimensions [7–10]. Specifically, the two-dimensional (2D) bulk state and one-dimensional (1D) edge state in 2D systems, as well as the three-dimensional (3D) bulk state, 2D surface state, and 1D hinge state (i.e., HOTS) in 3D systems, can all be localized to zero-dimensional (0D) states. The corner state (i.e., HOTS) in 2D and 3D systems can be transformed from multiple corner regions to a specific corner region. In contrast to the enhanced localization, the competition between the NHSE and the localization of topological states was considered recently [18–23]. This competition results in the dimensionality of the topological state increasing from lower to higher dimensions to achieve the delocalization (i.e., weakened localization). Furthermore, under specific parameters, the dimensionality of the topological state can become consistent with that of the bulk system (i.e., complete delocalization). Specifically, the edge states in 1D systems can be delocalized from 0D states to 1D states, while the corner states in 2D (3D) systems can be delocalized from 0D states to 2D (3D) states. The delocalization of topological states plays a crucial role in fundamental physics, such as the extended state in the band gap [18–21,23], the extended state in a localized continuum [22], and the bound state in the continuum [23]. Meanwhile, it shows extraordinary potential in applied physics, such as the application of topological states in adiabatic pumping [19], large-area topological lasers [18,20,21], coherent topological beam splitters [21], high energy capacity fibers [22], and topological sensors [22,23]. Therefore, the delocalization of topological states opens up a new avenue for exploring unique physical phenomena and designing innovative topological devices.

Different from crystals, 1D quasicrystals can be constructed from specific mathematical sequences or expressions [24]. 2D and 3D quasicrystals possess rotational symmetry, self-similarity, and long-range order [24–27]. Quasicrystals exhibit excellent optical localization and transmission characteristics [28,29] and present potential applications in optical fibers [28], magnetic quantum devices [30], and quantum transport [31]. The topology in quasicrystals has been theoretically and experimentally demonstrated [32,33], exhibiting unique geometric and physical properties, such as HOTSs with crystallographic forbidden symmetries (C_5, C_8, and C_{12} symmetries) [34–37], internal edge states [38] and HOTS arrays [39] that are difficult to realize in crystals, and topological superconductors without translational symmetry [40]. The non-Hermitian topological phase transition, localization, and delocalization in 1D quasicrystals have been found theoretically and experimentally [41–43], but higher-dimensional systems possess richer non-Hermitian phenomena and more flexible manipulations. The combination of 2D quasicrystals with the NHSE was recently proposed, leading to tunable

*Contact author: jianjun.liu@hnu.edu.cn

0D localized states [44,45]. However, this combination focused only on the enhanced localization without investigating delocalization and its mechanisms. Establishing a physical connection between 2D quasicrystals and the NHSE as well as delocalization remains a challenge. Topological effects in 3D quasicrystals (periodic stacking of 2D quasicrystals) have been proposed theoretically [46–49], but they are limited to Hermitian systems. The NHSE and delocalization in 3D quasicrystals remain unclear. Moreover, the combination of 3D quasicrystals with the NHSE could provide an opportunity to explore intriguing physical phenomena such as third-order skin states [12], Weyl exceptional rings [50], and third-order exceptional lines [51].

In this paper, we theoretically investigate the delocalization of HOTSs in 2D non-Hermitian quasicrystals, finding that these HOTSs exhibit delocalization distinct from that in non-Hermitian crystals. Through effective analysis of the quasicrystal boundaries, the physical connection between 2D quasicrystals and the NHSE as well as delocalization is revealed. Furthermore, by periodically stacking 2D non-Hermitian quasicrystals, we demonstrate the delocalization of HOTSs in 3D non-Hermitian quasicrystals and establish the connections between 3D quasicrystals, the NHSE, and topological effects.

II. TWO-DIMENSIONAL NON-HERMITIAN QUASICRYSTALS

The Stampfli-type quasicrystal and its energy spectrum are shown in Fig. 1. The Stampfli-type quasicrystal tiling can be formed by rhombi, regular triangles, and squares through iterative subdivision methods [52] (see Appendix A). The lattice site of a quasicrystal is used as a basic cell. By considering nearest- and next-nearest-neighbor hoppings, a tight-binding model for the Stampfli-type quasicrystal can be constructed, as illustrated in Fig. 1(b). The tight-binding Hamiltonian can be expressed as

$$H_{\text{2DStampfli}} = \sum_m c_m^\dagger (t_0 h_0 + g\tilde{h}_0) c_m + \sum_{m\neq n} c_m^\dagger t_1 h_1 c_n, \qquad (1)$$

where $c_m^\dagger$ represents the electron creation operator of basic cell m and c_m (c_n) represents the electron annihilation operator of basic cell m (n). h_0 (h_1) is determined by the reciprocal hopping within (between) basic cells. $h_0 = \tau_1\sigma_0 - \tau_2\sigma_2$, and $h_1 = (|\cos\theta_{mn}|\tau_1\sigma_0 - |\sin\theta_{mn}|\tau_2\sigma_2 + i\cos\theta_{mn}\tau_2\sigma_3 + i\sin\theta_{mn}\tau_2\sigma_1)e^{(1-r_{mn}/\xi)}/2$, where τ_j and σ_k ($j = 1, 2$; $k = 1, 2, 3$) are Pauli matrices for the degrees of freedom within a basic cell. σ_0 is the identity matrix. r_{mn} and θ_{mn} represent the distance between adjacent basic cells and the angle of the connecting lines of adjacent basic cells with respect to the horizontal direction, respectively. ξ is the decay length, and $\xi = 1$, which is consistent with the distance between next-nearest-neighbor basic cells. In the first term of Eq. (1), $g\tilde{h}_0$ represents the non-Hermitian part of the Hamiltonian, where g denotes the non-Hermitian strength. In the tight-binding model depicted in Fig. 1(b), the model is divided into nine regions, each with a distinct $\tilde{h}_0$. $\tilde{h}_0 = (a\tau_1\sigma_0 + b\tau_2\sigma_2 + ic\tau_2\sigma_3 + id\tau_2\sigma_1)/2$,where the coefficients (a, b, c, d) for regions A–H are distinct and are assigned as follows: $(1, -1, 1, -1)$, $(1, -1, -1, -1)$, $(1, -1, 1, 1)$, $(1, -1, -1, 1)$, $(0, -1, 0, -1)$, $(1, 0, 1, 0)$, $(1, 0, -1, 0)$, and $(0, -1, 0, 1)$. Region I, which contains the basic cell at the center of the structure, possesses only reciprocal hopping.

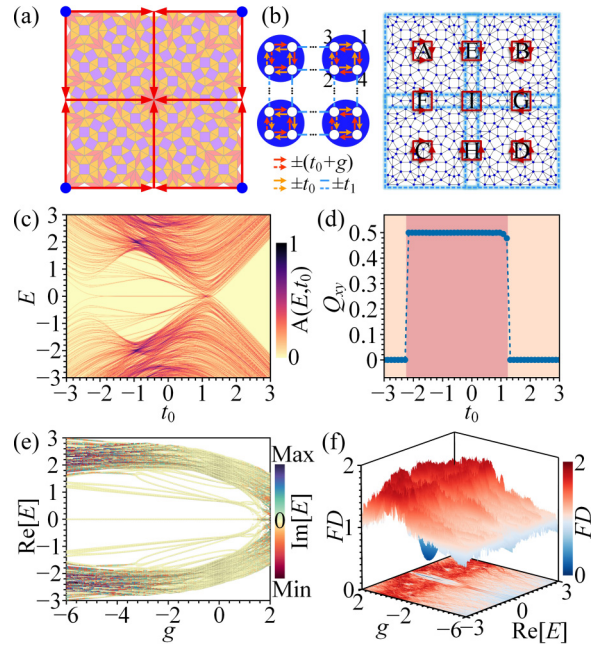

FIG. 1. Stampfli-type quasicrystal structure and its energy spectrum. (a) Schematics of the Stampfli-type quasicrystal tiling, HOTSs (blue dots), and delocalization directions (red arrows). (b) The tight-binding model. Left panel: four basic cells corresponding to HOTSs, with each cell consisting of four subsites. Right panel: the complete model, which is divided into nine regions (labeled as regions A–I), with red arrows indicating the direction of nonreciprocal hopping within each basic cell in regions A–H, while region I contains only reciprocal hopping. For the Hermitian case with $g = 0$, (c) the spectral function and (d) quadrupole moment as a function of t_0, calculated under the open boundary condition. (e) Eigenenergy and (f) fractal dimension of eigenstates as a function of g. Only 692 eigenstates with Re$[E] \in [-3, 3]$ are shown in (e) and (f). t_0 (t_1) and g represent the reciprocal and nonreciprocal hopping coefficients within (between) the basic cells, respectively.

$H_{\text{2DStampfli}}$ satisfies the sublattice symmetry S, mirror symmetries M_x and M_y, and rotational symmetry C_4 (see Appendix A). In the Hermitian case with $g = 0$, the model represents the extension of topological quadrupole insulators from crystals [53] to quasicrystals [35]. In the non-Hermitian case with $g \neq 0$, the model reflects the combination of the topological quadrupole insulator, quasicrystal, and nonreciprocal hopping. Figure 1(c) shows the spectral function [54] with $g = 0$ and $t_1 = 1.5$. The spectral function $A(E, t_0)$ can be expressed as

$$A(E, t_0) = -\text{ImTr}\{1/[E + i\eta - H_{\text{2DStampfli}}(t_0)]\}, \qquad (2)$$

where Im is the imaginary part, Tr is the trace of the matrix, E is the reference energy, and $\eta \to 0^+$. It can be seen from Fig. 1(c) that there are zero-energy states in the band gap with $t_0 \in [-2.2, 1.2]$. The real-space topological invariant (quadrupole moment Q_{xy}) is further calculated to characterize higher-order topology [55,56] (see Appendix B). The

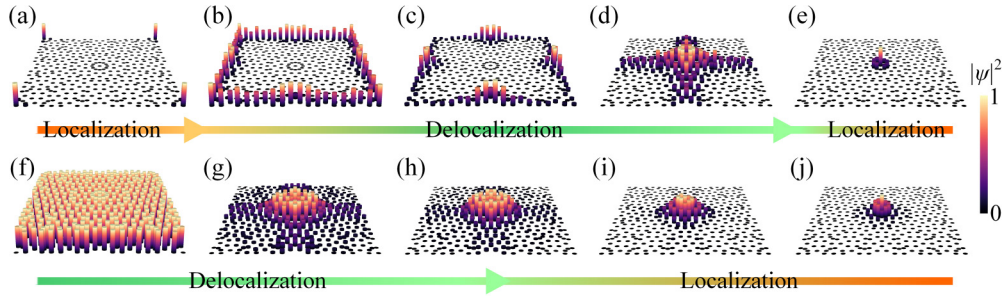

FIG. 2. Evolutions of wave function distributions corresponding to HOTSs and bulk states. The wave function distributions of (a)–(e) HOTSs and (f)–(j) bulk states vary with the parameter g. $g = 0$ in (a) and (f), $g = -1$ in (b) and (g), $g = -1.6$ in (c) and (h), $g = -2.65$ in (d) and (i), and $g = -6$ in (e) and (j). Other parameters are $t_1 = 1.5$ and $t_0 = -0.5$.

zero-energy states are robust against perturbations (see Appendix C). As can be seen from Fig. 1(d), within the range of the zero-energy states, the corresponding Q_{xy} is 0.5, while the rest are zero, which demonstrates that the zero-energy states are indeed HOTSs.

Considering the non-Hermitian case with $g \neq 0$ and $t_1 = 1.5$, we choose $t_0 = -0.5$ to obtain a larger band gap and calculate the energy spectrum as a function of g, as shown in Fig. 1(e). For $g \in (1.2, 2]$, the band gap vanishes, and the imaginary parts of the eigenenergies are nonzero. For $g \in [-6, 1.2]$, there are zero-energy states within the band gap, and their imaginary parts are zero. The non-Hermitian quadrupole moment $\tilde{Q}_{xy}$ is calculated [57,58] (see Appendix B). Within the range of zero-energy states, $\tilde{Q}_{xy}$ is 0.5. For $g \in (1.2, 2]$, there is no distinct band gap, and $\tilde{Q}_{xy}$ cannot be effectively calculated.

The presence of nonreciprocal hoppings can result in either enhanced localization or delocalization of HOTSs, and we focus on the latter. To effectively characterize the delocalization of HOTSs, we use the fractal dimension (FD) [59–61],

$$\mathrm{FD} = -\ln\left[\sum_m \sum_v \left|\psi^{\alpha}_{m,v}\right|^4\right] / \ln\sqrt{N}, \tag{3}$$

where $\psi^{\alpha}_{m,v}$ is the wave amplitude of the αth eigenstate at subsite v in basic cell m and N represents the total number of eigenstates, which is also the total number of subsites in the Stampfli-type quasicrystal. In our model, there are a total of 421 basic cells, each containing four subsites; thus, N equals 1684. The numerator of Eq. (3) represents the logarithm of the inverse participation ratio of the αth eigenstate. The inverse participation ratio reflects the localization degree of the eigenstate, with its value ranging from $1/N$ to 1 [62]. The square root of N in Eq. (3) represents the number of length subsites on one side. As shown in Fig. 1(f), when $g = 0$, the bulk states correspond to FD ≈ 2, and the HOTSs correspond to FD ≈ 0. Since t_0 is negative, we primarily consider the case where $g < 0$, such that $|t_0 + g| > |t_0|$. As g varies from 0 to -6, the nonreciprocity is enhanced, with the FD of the bulk states decreasing to about 0.9 and the FD of the HOTSs first increasing to about 1.4 before decreasing to about 0.7. Considering that the system is 2D, as the FD of the HOTSs increases from 0 to 1.4 and then decreases to 0.7, the corresponding order of the HOTSs decreases from 2 to 0.6 and then rises to 1.3, thereby indicating the phenomenon of fractional-order topological states.

The FD indicates that the wave function distributions of HOTSs and bulk states vary with the nonreciprocal parameter g. Some characteristic wave function distributions are selected (see Fig. 2). From Figs. 2(a)–2(e), with the enhancement of nonreciprocity, the HOTSs, initially localized at the four corner regions, delocalize along the boundaries of the quasicrystal [red arrows in Fig. 1(a)] and, ultimately, localize around region I. On the other hand, the bulk states exhibit an evolution from delocalization to localization, as shown in Figs. 2(f)–2(j). Additionally, it should be noted that in non-Hermitian crystals [21,22], the HOTSs did not delocalize along the boundary of the structure but delocalized throughout the bulk region. Therefore, the delocalization of HOTSs in quasicrystal differs from that in crystal, which is closely related to the unique lattice arrangement of a quasicrystal and its complex reciprocal and nonreciprocal hoppings. The delocalization of HOTSs in other noncrystalline systems, including fractals, amorphous structures, and other types of quasicrystals, is further discussed in Appendix D.

III. EFFECTIVE ANALYSIS OF THE QUASICRYSTAL BOUNDARIES

We further analyze the lattice arrangement of the outer boundary (see Fig. 3). It can be seen from Figs. 2(b) and 3(a) that the wave functions of the delocalized HOTSs are almost distributed on the outer boundary and bulk regions exhibit complex lattice arrangements. Therefore, the basic cell of the upper boundary in Fig. 3(b) is selected for effective analysis. The nonreciprocal hoppings can be divided into horizontal and vertical components [see Eq. (1)], which are represented by the green and orange arrows in Figs. 3(c) and 3(d), respectively. Unlike crystals, in which basic cells are arranged along the lattice vectors, the arrangement of basic cells in quasicrystals lacks a fixed direction. Therefore, the directions of the reciprocal hoppings between basic cells [green and orange lines in Figs. 3(c) and 3(d)] are not completely horizontal or vertical, and both directions need to be considered simultaneously.

We first consider the horizontal nonreciprocal hoppings, as shown in Fig. 3(c). Due to the sublattice symmetry of the system, in the Hermitian case, the HOTSs are localized at subsite 1 within each basic cell, and the wave function

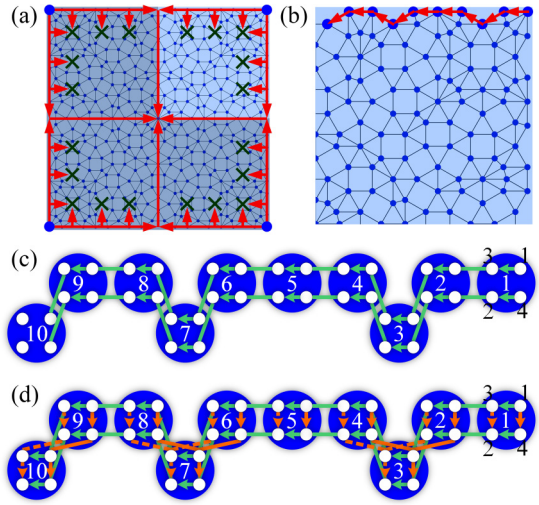

FIG. 3. Effective analysis of the quasicrystal boundary. (a) The tight-binding model and a schematic of delocalization. (b) The quarter sector in (a). The delocalization directions (suppressed delocalization directions) are shown by red arrows (black crosses). Schematics of the 10 basic cells [blue dots covered by red arrows in (b)] and their reciprocal and nonreciprocal hoppings: (c) nonreciprocal hoppings only along the horizontal direction (in green) and (d) nonreciprocal hoppings along both horizontal and vertical directions (in orange). The white and black numbers represent the serial numbers of the basic cells and the subsite indices within the basic cell, respectively.

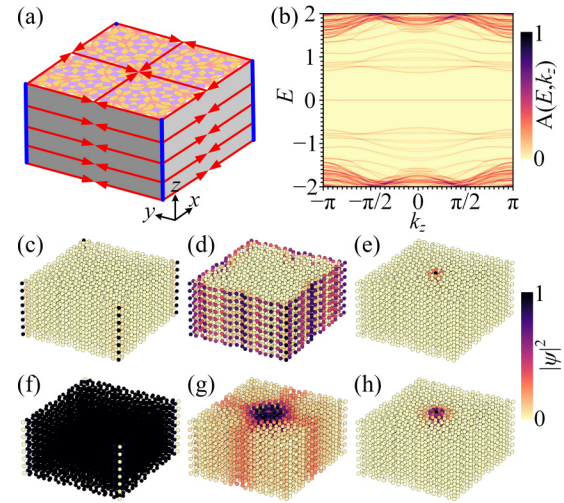

FIG. 4. Energy spectrum and evolutions of wave function distributions of a 3D quasicrystal. (a) Schematics of the 3D quasicrystal, HOTSs (blue hinges), and delocalization directions (red arrows). (b) Spectral function as a function of k_z with $g = -1.25$ under the open boundary condition in the xy plane and the periodic boundary condition along the z direction. (c)–(e) HOTSs and (f)–(h) bulk states as a function of g under the open boundary condition in all three directions (an eight-layer stack along z direction). $g = 0$ in (c) and (f), $g = -1.25$ in (d) and (g), and $g = -6$ in (e) and (h). Other parameters are $t_0 = -0.5$, $t_1 = 1.5$, and $t_2 = -0.25$.

amplitude exponentially decays from the first basic cell. In the non-Hermitian case, the decay trend of the wave function is altered by the nonreciprocal hoppings. The characteristic equation of the wave function [21,22] in Fig. 3(c) can be expressed as

$$E\psi_{m,3} = (t_0 + g)\psi_{m,1} - t_1 \cos\theta_{mm+1}\psi_{m+1,1}, \tag{4}$$

where $\psi_{m,v}$ represents the wave function amplitude with eigenenergy E. For $E = 0$, HOTSs correspond to $\psi_{m,v} = 0$ ($v \neq 1$). The ratio of the wave function amplitudes of neighboring subsites 1 is

$$\eta(\theta_{mm+1}) = \frac{\psi_{m,1}}{\psi_{m+1,1}} = \frac{t_1 \cos\theta_{mm+1}}{t_0 + g}. \tag{5}$$

Unlike the ratio in crystals [21,22], the ratio in quasicrystals is related to the angle θ_{mm+1}. The variation of $\eta(\theta_{mm+1})$ with θ_{mm+1} prevents $|\eta(\theta_{mm+1})|$ from being constantly 1, meaning that complete delocalization cannot be achieved. However, since $|\cos\theta_{mm+1}| \leqslant 1$, it is possible to attain $|\eta(\theta_{mm+1})| < 1$ when $|t_0 + g|$ is increased to the point where $|t_0 + g| > |t_1|$. The wave function amplitude transitions from a decaying to an increasing trend, shifting localization from the right end to the left end, which is accompanied by delocalization.

We further analyze the nonreciprocal hoppings in both the horizontal and vertical directions, as shown in Fig. 3(d). Taking basic cell 3 as an example, basic cell 2 is at the top right of it. Consequently, the directions of the nonreciprocal hoppings (in green and orange) are $2 \to 3$, and they are aligned with the direction of the red arrows in the corresponding region of Fig. 3(a) (i.e., towards the bottom left). Basic cell 4 is at the top left of basic cell 3, and the directions of the nonreciprocal hoppings indicated in green and orange are $3 \to 4$ and $4 \to 3$, respectively. These opposite tendencies mutually suppress each other. The arrangement of basic cells 1–10 is overall horizontal, and the delocalization starts from the first basic cell on the right. Therefore, the opposing tendencies primarily suppress the vertical direction and suppress the interaction between basic cell 3 and the basic cells below it. The situation for basic cell 7 is like that of basic cell 3, while basic cell 10 is not suppressed because it receives only the nonreciprocal hopping from basic cell 9 ($9 \to 10$). It can be understood that, apart from the leftmost basic cell 10, the wave function amplitudes in other basic cells struggle to delocalize further downward. The mirror and rotational symmetries satisfied by the system enable the above effective analysis to be applied to the remaining outer boundaries, as depicted by the red arrows and black crosses in Fig. 3(a).

IV. THREE-DIMENSIONAL NON-HERMITIAN QUASICRYSTALS

The 2D quasicrystal can be periodically stacked in the third dimension to form a 3D quasicrystal. We further explore the delocalization of HOTSs within a 3D quasicrystal (see Fig. 4). The effective Hamiltonian for the 3D quasicrystal in Fig. 4(a) can be constructed by adding the interlayer reciprocal hopping in the z direction to Eq. (1), which can be

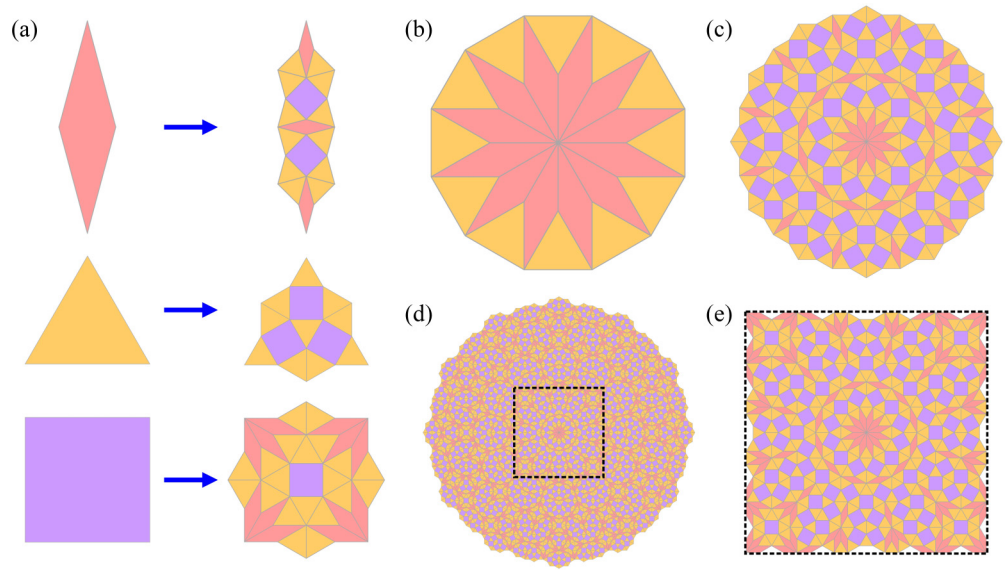

FIG. 5. Formation process of Stampfli-type quasicrystal tiling. (a) Three primitive tiles and their subdivision methods. (b) Initial tiling of the Stampfli-type quasicrystal. (c) One iteration. (d) Two iterations. (e) The tiling corresponding to the black dashed box in (d).

expressed as

$$H_{\mathrm{3DStampfli}} = H_{\mathrm{2DStampfli}} + \sum_m c_m^\dagger 2t_2 \cos k_z h_0 c_m, \qquad (6)$$

where t_2 is the interlayer reciprocal hopping coefficient. $H_{\mathrm{3DStampfli}}$ also satisfies the sublattice symmetry S, mirror symmetries M_x and M_y, and rotational symmetry C_4 (see Appendix A). In the non-Hermitian case with $g \neq 0$, the model exhibits a combination of the NHSE [7,8] and 3D topological quasicrystals [46–49]. As depicted by the spectral function $A(E, k_z)$ in Fig. 4(b), zero-energy states exist within the band gap, and calculations reveal the corresponding $\tilde{Q}_{xy}$ is 0.5. As g varies from 0 to -1.25, the nonreciprocal hoppings cause the HOTSs (hinge states) to delocalize into surface states, while bulk states localize towards the center, as shown in Figs. 4(c), 4(d), 4(f), and 4(g). With further enhancement of the nonreciprocal hoppings, at $g = -6$, both topological states and bulk states localize in the center of the structure, as depicted in Figs. 4(e) and 4(h).

V. CONCLUSIONS

In summary, we theoretically demonstrated the delocalization of HOTSs induced by the NHSE in 2D and 3D quasicrystals. We established the physical connection between higher-dimensional quasicrystals and NHSE as well as delocalization. The HOTSs in quasicrystals exhibit the characteristic of delocalization along the boundaries rather than in the bulk regions, and it was effectively characterized through the analysis of quasicrystal boundaries. The delocalization of HOTSs provides a different approach for manipulating the propagation of light, which can be used to design innovative topological devices such as large-area topological lasers [18,20,21] and coherent topological beam splitters [21]. Our results not only generalize to other quasicrystals, such as Penrose-type and Ammann-Beenker-type quasicrystals, but also provide valuable insights into the exploration of novel physical phenomena in noncrystalline systems, including fractals and amorphous structures.

ACKNOWLEDGMENTS

This work was supported by the National Natural Science Foundation of China (Grants No. 61405058 and No. 62075059), the Natural Science Foundation of Hunan Province (Grants No. 2017JJ2048 and No. 2020JJ4161), the Scientific Research Foundation of Hunan Provincial Education Department (Grant No. 21A0013), the Open Project of the State Key Laboratory of Advanced Optical Communication Systems and Networks of China (Grant No. 2024GZKF20), and the Guangdong Basic and Applied Basic Research Foundation (Grant No. 2024A1515011353).

APPENDIX A: TILING CONSTRUCTION AND SYMMETRY ANALYSIS OF STAMPFLI-TYPE QUASICRYSTALS

The iterative subdivision method [52] is used to construct the Stampfli-type quasicrystal tiling (see Fig. 5). The subdivision methods for a rhombus, a regular triangle, and a square are shown in Fig. 5(a). The rhombus is subdivided into 3 small rhombuses, 12 small regular triangles, and 2 small squares. The regular triangle is subdivided into 10 small regular triangles and 3 small squares. The square is subdivided into 12 small rhombuses, 20 small regular triangles, and 1 small square. According to this subdivision method, by performing one and two iterations of the primitive tiles at the corresponding position in Fig. 5(b), the Stampfli-type quasicrystal tilings shown in Figs. 5(c) and 5(d) can be obtained, respectively. Considering the further construction and study of 2D and 3D Stampfli-type non-Hermitian quasicrystals, only the tiling corresponding to the black dashed box in Fig. 5(d) is selected as the research object, as shown in Fig. 5(e).

Based on the quasicrystal tiling, the tight-binding model and effective Hamiltonian of Stampfli-type quasicrystal can

be constructed. We further discuss the symmetries satisfied by the effective Hamiltonian of the Stampfli-type quasicrystal. $H_{2\text{DStampfli}}$ [see Eq. (1)] and $H_{3\text{DStampfli}}$ [see Eq. (6)] of Stampfli-type quasicrystals satisfy the sublattice symmetry S and spatial symmetries (including mirror symmetries M_x and M_y and rotational symmetry C_4) [7,35], which can be expressed as

$$SH_{2\text{D(3D)Stampfli}}S^{-1} = -H_{2\text{D(3D)Stampfli}}, \tag{A1}$$

$$M_xH_{2\text{D(3D)Stampfli}}M_x^{-1} = H_{2\text{D(3D)Stampfli}}, \tag{A2}$$

$$M_yH_{2\text{D(3D)Stampfli}}M_y^{-1} = H_{2\text{D(3D)Stampfli}}, \tag{A3}$$

$$C_4H_{2\text{D(3D)Stampfli}}C_4^{-1} = H_{2\text{D(3D)Stampfli}}, \tag{A4}$$

where $S = \tau_3\sigma_0$, $M_x = \tau_1\sigma_3U_x$, $M_y = \tau_1\sigma_1U_y$, $C_4 = R_1U_4$, and $R_4 = [(\tau_1 - i\tau_2)\sigma_0 + (\tau_1 + i\tau_2)(i\sigma_2)]/2$. τ_k and σ_k ($k = 1, 2, 3$) are Pauli matrices for the degrees of freedom within a basic cell. σ_0 is the identity matrix. $U_{x,y}$ are orthogonal matrices permuting the lattice sites of the tiling to flip the whole system vertically and horizontally. U_4 is an orthogonal matrix permuting the lattice sites of the tiling to rotate the whole system by $\pi/2$. Moreover, $H_{2\text{DStampfli}}$ and $H_{3\text{DStampfli}}$ satisfy the combined symmetries C_4M_x and C_4M_y [7,35], which can be expressed as

$$C_4M_xH_{2\text{D(3D)Stampfli}}(C_4M_x)^{-1} = H_{2\text{D(3D)Stampfli}}, \tag{A5}$$

$$C_4M_yH_{2\text{D(3D)Stampfli}}(C_4M_y)^{-1} = H_{2\text{D(3D)Stampfli}}. \tag{A6}$$

APPENDIX B: QUADRUPOLAR MOMENT AND NON-HERMITIAN QUADRUPOLE MOMENT

In this Appendix, we present the real-space topological invariants for the Hermitian system (quadrupole moment Q_{xy}) [55,56] and the non-Hermitian system (non-Hermitian quadrupole moment $\tilde{Q}_{xy}$) [57,58]. $Q_{xy} = 0.5$ and $\tilde{Q}_{xy} = 0.5$ correspond to the higher-order topological phase. $Q_{xy} = 0$ and $\tilde{Q}_{xy} = 0$ correspond to the trivial phase. First, considering the Hermitian case [55,56], Q_{xy} can be expressed as

$$Q_{xy} = q - q_{\text{al}} (\text{mod } 1), \tag{B1}$$

where q and q_{al} are

$$q = -\frac{i}{2\pi}\text{Tr}[\ln(U^\dagger OU)], \quad O = \exp\left[\frac{2\pi i}{L_xL_y}\sum_m m_xm_y\right], \tag{B2}$$

$$q_{\text{al}} = \sum_m m_xm_y/(L_xL_y), \tag{B3}$$

where U is constructed by columnwise arrangement of the eigenvectors for the negative-energy filled states. m is the serial number of the basic cell. m_x (L_x) and m_y (L_y) are the coordinates (sample size) along the x and y directions, respectively. q_{al} represents q in the atomic limit and at half filling.

Unlike in Hermitian systems, non-Hermitian systems involve a right eigenvector $|u_R\rangle$ and a left eigenvector $|u_L\rangle$ [2], which can be expressed as

$$H_{2\text{D(3D)Stampfli}}|u_R\rangle = E|u_R\rangle, \tag{B4}$$

$$H^\dagger_{2\text{D(3D)Stampfli}}|u_L\rangle = E^*|u_L\rangle. \tag{B5}$$

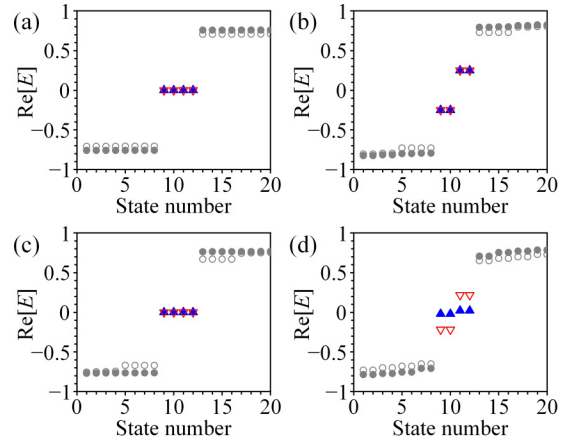

FIG. 6. Robustness of the HOTSs against perturbations. Types of perturbations: (a) Δh_1, (b) Δh_2, (c) Δh_3, and (d) Δh_4. Only 20 eigenstates close to zero energy are illustrated in (a)–(d). Gray dots (blue triangles) represent the bulk states (HOTSs) calculated by $H_{2\text{DStampfli}}$, and gray hollow circles (red hollow triangles) represent the bulk states (HOTSs) calculated by $H_{3\text{DStampfli}}$. Parameters are $g = -1.25$, $t_0 = -0.5$, $t_1 = 1.5$, $t_2 = -0.25$, $t_3 = -0.25$, and $w_m \in [-1, 1]$. $k_z = \pi$ in $H_{3\text{DStampfli}}$.

The non-Hermitian quadrupole moment $\tilde{Q}_{xy}$ is extended from the Hermitian quadrupole moment Q_{xy} [57,58],

$$\tilde{Q}_{xy} = \tilde{q} - q_{\text{al}} (\text{mod } 1), \tag{B6}$$

where q_{al} is consistent with Eq. (B3). $\tilde{q}$, based on Eq. (B2), is extended to a non-Hermitian biorthogonal basis and can be expressed as

$$\tilde{q} = -\frac{i}{2\pi}\text{Tr}[\ln(U_L^\dagger OU_R)], \tag{B7}$$

where O is consistent with Eq. (B2). U_L (U_R) is constructed by columnwise arrangement of the left (right) eigenvectors for the negative-energy filled states.

APPENDIX C: ROBUSTNESS AGAINST PERTURBATIONS

In this Appendix, we discuss the stability (i.e., robustness against perturbations) of the zero-energy states (i.e., HOTSs) in the energy spectrum when perturbation terms are introduced into $H_{2\text{DStampfli}}$ and $H_{3\text{DStampfli}}$. First, we consider two types of perturbations [35], which can be expressed as

$$\Delta h_1 = \sum_m t_3 c_m^\dagger \tau_0\sigma_2 c_m, \tag{C1}$$

$$\Delta h_2 = \sum_m t_3 c_m^\dagger \tau_3\sigma_0 c_m. \tag{C2}$$

Equations (C1) and (C2) are applied to $H_{2\text{DStampfli}}$ and $H_{3\text{DStampfli}}$, altering the reciprocal and nonreciprocal hoppings within the basic cells, with a perturbation coefficient $t_3 = -0.25$. The energy spectra after introducing perturbation are shown in Fig. 6.

The perturbation term Δh_1 breaks the mirror symmetries M_x and M_y while maintaining the rotational symmetry C_4, allowing the four HOTSs to remain stably degenerate at zero energy, as shown in Fig. 6(a). The perturbation term Δh_2

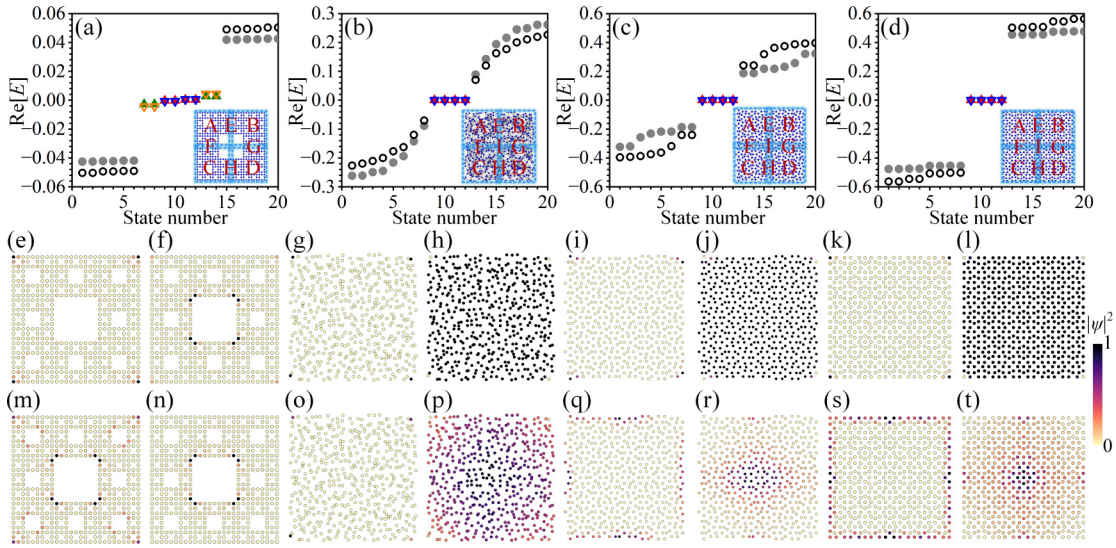

FIG. 7. Delocalization of HOTSs in other noncrystalline systems. Energy spectrum for (a) a Sierpiński carpet fractal with 512 basic cells, (b) an amorphous structure with 484 randomly distributed basic cells, (c) a Penrose-type quasicrystal with 476 basic cells, and (d) an Ammann-Beenker-type quasicrystal with 513 basic cells. The insets show the schematics of these noncrystalline structures. Only 20 eigenstates close to zero energy are illustrated. The Sierpiński carpet fractal in (a) possesses two types of HOTSs, represented by red and green triangles for the Hermitian case with $g = 0$ and blue and yellow hollow triangles for the non-Hermitian case with $g \neq 0$. The remaining eigenstates are represented by gray dots (black hollow circles) for the Hermitian (non-Hermitian) case. In (b)–(d), the HOTSs are represented by red triangles (blue hollow triangles) for the Hermitian (non-Hermitian) case. The bulk states are represented by gray dots (black hollow circles) for the Hermitian (non-Hermitian) case. The wave function distributions of HOTSs and bulk states for (e)–(l) the Hermitian case and (m)–(t) the non-Hermitian case.

breaks both mirror and rotational symmetries, causing the HOTSs to no longer be degenerate at zero energy, as shown in Fig. 6(b). We further consider the varying perturbation coefficients, which can be expressed as

$$\Delta h_3 = \sum_m t_3 w_m c_m^\dagger \tau_0 \sigma_2 c_m, \tag{C3}$$

$$\Delta h_4 = \sum_m t_3 w_m c_m^\dagger \tau_3 \sigma_0 c_m. \tag{C4}$$

Compared to Eqs. (C1) and (C2), Eqs. (C3) and (C4) have taken into account the perturbations that vary randomly with the basic cell m, with $t_3 = -0.25$ and $w_m \in [-1, 1]$. It should be noted that Δh_3 is set to maintain the rotational symmetry C_4 by assigning random values only in the top right quarter of the quasicrystal, while the other three quarters are generated in correspondence with C_4. In contrast, Δh_4 is not restricted by rotational symmetry. As can be seen from Figs. 6(c) and 6(d), in the case of Δh_3, the four HOTSs remain stably degenerate at zero energy, whereas in the case of Δh_4, the HOTSs are gapped out. In Figs. 6(c) and 6(d), although the perturbation terms affect the degeneracy of the HOTSs, the band gap still exists, indicating that the system remains topological.

APPENDIX D: DELOCALIZATION OF HOTSS IN OTHER NONCRYSTALLINE SYSTEMS

In this Appendix, the delocalization of HOTSs is extended to other noncrystalline systems, including Sierpiński carpet fractals [56,59,60], amorphous structures, and Penrose-type and Ammann-Beenker-type quasicrystals, as shown in Fig. 7.

In order to construct the tight-binding model of a Sierpiński carpet fractal, the lattice sites of the fractal are used as basic cells, and each basic cell contains four subsites, which is consistent with the construction method of basic cells and subsites in Stampfli-type quasicrystals. The tight-binding model is depicted in Fig. 7(a). The tight-binding Hamiltonian H_{fractal} of the fractal has the same form as $H_{\text{2DStampfli}}$ [see Eq. (1)] of Stampfli-type quasicrystals. However, due to the different lattice arrangements between the fractal and the Stampfli-type quasicrystal, there are also differences between H_{fractal} and $H_{\text{2DStampfli}}$: (1) For H_{fractal}, we consider only nearest-neighbor hoppings, so h_1 in H_{fractal} does not have a spatial decay factor, i.e., $h_1 = (|\cos\theta_{mn}|\tau_1\sigma_0 - |\sin\theta_{mn}|\tau_2\sigma_2 + i\cos\theta_{mn}\tau_2\sigma_3 + i\sin\theta_{mn}\tau_2\sigma_1)/2$. (2) Since there are no lattice sites in the central region of the fractal, the tight-binding model of the fractal includes only regions A–H and not region I.

Considering the Hermitian case with $g = 0$, $t_0 = 0.45$, and $t_1 = 1.5$, we solve the Hamiltonian H_{fractal} to obtain the energy spectrum. As shown in Fig. 7(a), there are two types of near-zero-energy eigenstates, marked by red and green triangles. Previous works showed that both types of eigenstates are HOTSs [56,59,60], with their wave functions localized in the outer and inner corner regions of the fractal, as illustrated in Figs. 7(e) and 7(f), respectively. For the non-Hermitian case with $g = 0.08$, the HOTSs still exist, as shown by the blue and yellow hollow triangles in Fig. 7(a). The NHSE leads to the delocalization of HOTSs that are localized in the outer corner regions along the diagonal towards the inner corner regions,

whereas the HOTSs that are localized in the inner corner regions remain basically unchanged, as shown in Figs. 7(m) and 7(n).

We further investigate the HOTSs and NHSE in the amorphous structure. We introduce randomly distributed lattice sites within a square region of dimensions $L_x = L_y = 22$ to construct an amorphous structure. The lattice sites are used as basic cells, and each basic cell contains four subsites. The tight-binding model is depicted in Fig. 7(b). The tight-binding Hamiltonian $H_{\text{amorphous}}$ of amorphous structure has the same form as $H_{\text{2DStampfli}}$ [see Eq. (1)] of Stampfli-type quasicrystals. However, as there are no nearest- and next-nearest-neighbor hoppings in the amorphous structure, h_1 in $H_{\text{amorphous}}$ differs from that in $H_{\text{2DStampfli}}$. Specifically, $h_1 = (|\cos\theta_{mn}|\tau_1\sigma_0 - |\sin\theta_{mn}|\tau_2\sigma_2 + i\cos\theta_{mn}\tau_2\sigma_3 + i\sin\theta_{mn}\tau_2\sigma_1)\Theta(R - r_{mn})e^{(1-r_{mn}/\xi)}/2$. Θ is the step function, and R controls the range of hopping [40]. We consider only the hoppings between basic cells with $r_{mn} < R$ and set R to be twice the value of the decay length ξ, that is, $R = 2$. The tight-binding model of the amorphous structure also contains nine regions (i.e., regions A–I), which is consistent with that in Stampfli-type quasicrystal.

Considering the Hermitian case with $g = 0$, $t_0 = 0.3$, and $t_1 = 1.5$, we solve the Hamiltonian $H_{\text{amorphous}}$ to obtain the energy spectrum, as shown in Fig. 7(b). The wave function distributions of the zero-energy eigenstates (red triangles) are depicted in Fig. 7(g), and Q_{xy} is calculated as 0.5, revealing that these eigenstates are HOTSs. The wave function distributions of the bulk states are extended, as illustrated in Fig. 7(h). For the non-Hermitian case with $g = 0.08$, the HOTSs do not delocalize, and the bulk states localize towards the center of the structure, as shown in Figs. 7(o) and 7(p). The suppression of the delocalization of HOTSs is related to the complex lattice arrangement and hoppings in amorphous structure. Based on the effective analysis of boundaries in Stampfli-type quasicrystal and Eqs. (4) and (5), the nonreciprocal hoppings in different directions suppress the delocalization of HOTSs. As can be seen from the tight-binding model in Fig. 7(b), the lattice sites on the boundaries and in the bulk regions of the amorphous structure have multiple-directional and complex hoppings, thereby suppressing the delocalization of HOTSs. Therefore, the combination of HOTSs and the NHSE in the fractal and amorphous structure exhibits different physical properties from those of the Stampfli-type quasicrystal.

The tight-binding Hamiltonian of Stampfli-type quasicrystals is further extended to Penrose-type and Ammann-Beenker-type quasicrystals. The quasicrystal lattices are constructed according to the Penrose-type and Ammann-Beenker-type tilings [52]. The lattice sites of the two quasicrystals are used as the basic cells, and each basic cell contains four subsites. The tight-binding Hamiltonians H_{Penrose} and $H_{\text{Ammann-Beenker}}$ of two quasicrystals both have the same form as $H_{\text{2DStampfli}}$ [see Eq. (1)] of Stampfli-type quasicrystals. The tight-binding models are depicted in Figs. 7(c) and 7(d). We consider the first three nearest neighbors in the tight-binding models. Specifically, in the Penrose-type quasicrystal, we consider the hoppings along the edges or short diagonals of the rhombuses, and in the Ammann-Beenker-type quasicrystal, we consider the hoppings along the edges or diagonals (short diagonals) of the square (rhombus). The tight-binding models of the two quasicrystals are also divided into nine regions.

Considering the Hermitian case with $g = 0$, $t_1 = 1.5$, and $t_0 = -0.6$ and -0.5, we solve H_{Penrose} and $H_{\text{Ammann-Beenker}}$ to obtain the energy spectra of the two quasicrystals, as depicted in Figs. 7(c) and 7(d), respectively. The wave function distributions of the zero-energy eigenstates (red triangles) are shown in Figs. 7(i) and 7(k), respectively, and Q_{xy} is calculated as 0.5, revealing that these eigenstates are HOTSs. The wave function distributions of the bulk states are extended, as illustrated in Figs. 7(j) and 7(l), respectively. Considering the non-Hermitian cases with $g = -0.9$ and -1, the wave function distributions of the HOTSs and bulk states for the two quasicrystals are shown in Figs. 7(q)–7(t). The HOTSs of the two quasicrystals both delocalize along the boundaries, and the bulk states localize to the central region of the structure. Therefore, both the Penrose-type and Ammann-Beenker-type quasicrystals possess delocalization of HOTSs similar to that of the Stampfli-type quasicrystal, which demonstrates the universality of our results in quasicrystals.

[1] E. J. Bergholtz, J. C. Budich, and F. K. Kunst, Exceptional topology of non-Hermitian systems, Rev. Mod. Phys. **93**, 015005 (2021).

[2] S. Yao and Z. Wang, Edge states and topological invariants of non-Hermitian systems, Phys. Rev. Lett. **121**, 086803 (2018).

[3] F. K. Kunst, E. Edvardsson, J. C. Budich, and E. J. Bergholtz, Biorthogonal bulk-boundary correspondence in non-Hermitian systems, Phys. Rev. Lett. **121**, 026808 (2018).

[4] N. Okuma, K. Kawabata, K. Shiozaki, and M. Sato, Topological origin of non-Hermitian skin effects, Phys. Rev. Lett. **124**, 086801 (2020).

[5] X. Zhang, T. Zhang, M.-H. Lu, and Y.-F. Chen, A review on non-Hermitian skin effect, Adv. Phys. X **7**, 2109431 (2022).

[6] R. Lin, T. Tai, L. Li, and C. H. Lee, Topological non-Hermitian skin effect, Front. Phys. **18**, 53605 (2023).

[7] T. Liu, Y.-R. Zhang, Q. Ai, Z. Gong, K. Kawabata, M. Ueda, and F. Nori, Second-order topological phases in non-Hermitian systems, Phys. Rev. Lett. **122**, 076801 (2019).

[8] C. H. Lee, L. Li, and J. Gong, Hybrid higher-order skin-topological modes in nonreciprocal systems, Phys. Rev. Lett. **123**, 016805 (2019).

[9] Y. Li, C. Liang, C. Wang, C. Lu, and Y.-C. Liu, Gain-loss-induced hybrid skin-topological effect, Phys. Rev. Lett. **128**, 223903 (2022).

[10] H. Liu and I. C. Fulga, Mixed higher-order topology: Boundary non-Hermitian skin effect induced by a Floquet bulk, Phys. Rev. B **108**, 035107 (2023).

[11] L. S. Palacios, S. Tchoumakov, M. Guix, I. Pagonabarraga, S. Sánchez, and A. G. Grushin, Guided accumulation of active particles by topological design of a second-order skin effect, Nat. Commun. **12**, 4691 (2021).

[12] D. Zou, T. Chen, W. He, J. Bao, C. H. Lee, H. Sun, and X. Zhang, Observation of hybrid higher-order skin-topological effect in non-Hermitian topolectrical circuits, Nat. Commun. **12**, 7201 (2021).

[13] C. Shang, S. Liu, R. Shao, P. Han, X. Zang, X. Zhang, K. N. Salama, W. Gao, C. H. Lee, R. Thomale, A. Manchon, S. Zhang, T. J. Cui, and U. Schwingenschlögl, Experimental identification of the second-order non-Hermitian skin effect with physics-graph-informed machine learning, Adv. Sci. **9**, 2202922 (2022).

[14] X. Zhang, Y. Tian, J.-H. Jiang, M.-H. Lu, and Y.-F. Chen, Observation of higher-order non-Hermitian skin effect, Nat. Commun. **12**, 5377 (2021).

[15] Z. Gao, X. Qiao, M. Pan, S. Wu, J. Yim, K. Chen, B. Midya, L. Ge, and L. Feng, Two-dimensional reconfigurable non-Hermitian gauged laser array, Phys. Rev. Lett. **130**, 263801 (2023).

[16] Y. Sun, X. Hou, T. Wan, F. Wang, S. Zhu, Z. Ruan, and Z. Yang, Photonic Floquet skin-topological effect, Phys. Rev. Lett. **132**, 063804 (2024).

[17] G.-G. Liu, S. Mandal, P. Zhou, X. Xi, R. Banerjee, Y.-H. Hu, M. Wei, M. Wang, Q. Wang, Z. Gao, H. Chen, Y. Yang, Y. Chong, and B. Zhang, Localization of chiral edge states by the non-Hermitian skin effect, Phys. Rev. Lett. **132**, 113802 (2024).

[18] S. Longhi, Non-Hermitian gauged topological laser arrays, Ann. Phys. (Berlin, Ger.) **530**, 1800023 (2018).

[19] W. Zhu, W. X. Teo, L. Li, and J. Gong, Delocalization of topological edge states, Phys. Rev. B **103**, 195414 (2021).

[20] W. X. Teo, W. Zhu, and J. Gong, Tunable two-dimensional laser arrays with zero-phase locking, Phys. Rev. B **105**, L201402 (2022).

[21] W. Wang, X. Wang, and G. Ma, Non-Hermitian morphing of topological modes, Nature (London) **608**, 50 (2022).

[22] W. Wang, X. Wang, and G. Ma, Extended state in a localized continuum, Phys. Rev. Lett. **129**, 264301 (2022).

[23] M. Zelenayova and E. J. Bergholtz, Non-Hermitian extended midgap states and bound states in the continuum, Appl. Phys. Lett. **124**, 041105 (2024).

[24] C. Janot, *Quasicrystals: A Primer*, 2nd ed. (Clarendon, Oxford, 1994).

[25] D. Shechtman, I. Blech, D. Gratias, and J. W. Cahn, Metallic phase with long-range orientational order and no translational symmetry, Phys. Rev. Lett. **53**, 1951 (1984).

[26] D. Levine and P. J. Steinhardt, Quasicrystals. I. Definition and structure, Phys. Rev. B **34**, 596 (1986).

[27] J. E. S. Socolar and P. J. Steinhardt, Quasicrystals. II. Unit-cell configurations, Phys. Rev. B **34**, 617 (1986).

[28] E. Liu and J. Liu, Quasiperiodic photonic crystal fiber, Chin. Opt. Lett. **21**, 060603 (2023).

[29] P. Wang, Q. Fu, V. V. Konotop, Y. V. Kartashov, and F. Ye, Observation of localization of light in linear photonic quasicrystals with diverse rotational symmetries, Nat. Photon. **18**, 224 (2024).

[30] A. Lopez-Bezanilla and C. Nisoli, Field-induced magnetic phases in a qubit Penrose quasicrystal, Sci. Adv. **9**, eadf6631 (2023).

[31] T. Shimasaki, M. Prichard, H. E. Kondakci, J. E. Pagett, Y. Bai, P. Dotti, A. Cao, A. R. Dardia, T.-C. Lu, T. Grover, and D. M. Weld, Anomalous localization in a kicked quasicrystal, Nat. Phys. **20**, 409 (2024).

[32] O. Zilberberg, Topology in quasicrystals, Opt. Mater. Express **11**, 1143 (2021).

[33] J. Fan and H. Huang, Topological states in quasicrystals, Front. Phys. **17**, 13203 (2022).

[34] D. Varjas, A. Lau, K. Pöyhönen, A. R. Akhmerov, D. I. Pikulin, and I. C. Fulga, Topological phases without crystalline counterparts, Phys. Rev. Lett. **123**, 196401 (2019).

[35] R. Chen, C.-Z. Chen, J.-H. Gao, B. Zhou, and D.-H. Xu, Higher-order topological insulators in quasicrystals, Phys. Rev. Lett. **124**, 036803 (2020).

[36] C.-B. Hua, R. Chen, B. Zhou, and D.-H. Xu, Higher-order topological insulator in a dodecagonal quasicrystal, Phys. Rev. B **102**, 241102(R) (2020).

[37] C. Wang, F. Liu, and H. Huang, Effective model for fractional topological corner modes in quasicrystals, Phys. Rev. Lett. **129**, 056403 (2022).

[38] C. W. Duncan, S. Manna, and A. E. B. Nielsen, Topological models in rotationally symmetric quasicrystals, Phys. Rev. B **101**, 115413 (2020).

[39] A. Shi, Y. Peng, J. Jiang, Y. Peng, P. Peng, J. Chen, H. Chen, S. Wen, X. Lin, F. Gao, and J. Liu, Observation of topological corner state arrays in photonic quasicrystals, Laser Photon. Rev. **18**, 2300956 (2024).

[40] S. Manna, S. K. Das, and B. Roy, Noncrystalline topological superconductors, Phys. Rev. B **109**, 174512 (2024).

[41] S. Longhi, Topological phase transition in non-Hermitian quasicrystals, Phys. Rev. Lett. **122**, 237601 (2019).

[42] Q. Lin, T. Li, L. Xiao, K. Wang, W. Yi, and P. Xue, Topological phase transitions and mobility edges in non-Hermitian quasicrystals, Phys. Rev. Lett. **129**, 113601 (2022).

[43] S. Weidemann, M. Kremer, S. Longhi, and A. Szameit, Topological triple phase transition in non-Hermitian Floquet quasicrystals, Nature (London) **601**, 354 (2022).

[44] J. Chen, A. Shi, Y. Peng, P. Peng, and J. Liu, Hybrid skin-topological effect induced by eight-site cells and arbitrary adjustment of the localization of topological edge states, Chin. Phys. Lett. **41**, 037103 (2024).

[45] C. Rangi, K.-M. Tam, and J. Moreno, Engineering a non-Hermitian second-order topological insulator state in quasicrystals, Phys. Rev. B **109**, 064203 (2024).

[46] A. Grossi e Fonseca, T. Christensen, J. D. Joannopoulos, and M. Soljačić, Quasicrystalline Weyl points and dense Fermi-Bragg arcs, Phys. Rev. B **108**, L121109 (2023).

[47] R. Chen, B. Zhou, and D.-H. Xu, Quasicrystalline second-order topological semimetals, Phys. Rev. B **108**, 195306 (2023).

[48] Y.-F. Mao, Y.-L. Tao, J.-H. Wang, Q.-B. Zeng, and Y. Xu, Higher-order topological insulators in three dimensions without crystalline counterparts, Phys. Rev. B **109**, 134205 (2024).

[49] Z.-G. Chen, C. Lou, K. Hu, and L.-K. Lim, Fractal surface states in three-dimensional topological quasicrystals, arXiv:2401.11497.

[50] J.-J. Liu, Z.-W. Li, Z.-G. Chen, W. Tang, A. Chen, B. Liang, G. Ma, and J.-C. Cheng, Experimental realization of Weyl exceptional rings in a synthetic three-dimensional non-Hermitian phononic crystal, Phys. Rev. Lett. **129**, 084301 (2022).

[51] W. Tang, K. Ding, and G. Ma, Realization and topological properties of third-order exceptional lines embedded in exceptional surfaces, Nat. Commun. **14**, 6660 (2023).

[52] D. Frettlöh, F. Gähler, and E. Harriss, Tilings Encyclopedia, https://tilings.math.uni-bielefeld.de/.

[53] W. A. Benalcazar, B. A. Bernevig, and T. L. Hughes, Quantized electric multipole insulators, Science **357**, 61 (2017).

[54] T. Wan, K. Zhang, J. Li, Z. Yang, and Z. Yang, Observation of the geometry-dependent skin effect and dynamical degeneracy splitting, Sci. Bull. **68**, 2330 (2023).

[55] W. A. Wheeler, L. K. Wagner, and T. L. Hughes, Many-body electric multipole operators in extended systems, Phys. Rev. B **100**, 245135 (2019).

[56] S. Manna, S. Nandy, and B. Roy, Higher-order topological phases on fractal lattices, Phys. Rev. B **105**, L201301 (2022).

[57] S. A. A. Ghorashi, T. Li, M. Sato, and T. L. Hughes, Non-Hermitian higher-order Dirac semimetals, Phys. Rev. B **104**, L161116 (2021).

[58] S. Manna and B. Roy, Inner skin effects on non-Hermitian topological fractals, Commun. Phys. **6**, 10 (2023).

[59] J. Li, Q. Mo, J.-H. Jiang, and Z. Yang, Higher-order topological phase in an acoustic fractal lattice, Sci. Bull. **67**, 2040 (2022).

[60] S. Zheng, X. Man, Z.-L. Kong, Z.-K. Lin, G. Duan, N. Chen, D. Yu, J.-H. Jiang, and B. Xia, Observation of fractal higher-order topological states in acoustic metamaterials, Sci. Bull. **67**, 2069 (2022).

[61] Z. Ou, Y. Wang, and L. Li, Non-Hermitian boundary spectral winding, Phys. Rev. B **107**, L161404 (2023).

[62] D. J. Thouless, Electrons in disordered systems and the theory of localization, Phys. Rep. **13**, 93 (1974).